# SnO₂–Au hybrid nanoparticles as effective catalysts for oxygen electroreduction in alkaline media

Wei Chen, David Ny, Shaowei Chen *

*Department of Chemistry and Biochemistry, University of California, 1156 High Street, Santa Cruz, CA 95064, USA*

## ARTICLE INFO

## ABSTRACT

SnO₂ nanoparticles were synthesized by a facile electrochemical method based on anodic oxidation of a tin metal sheet. The resulting particles, with an average diameter of about 20 nm, were then loaded with varied amounts of HAuCl₄, forming SnO₂–Au($x$) ($x$ = 0, 0.095, 0.38, 0.76, 1.9, 3.0, and 3.8 at.%) hybrid nanoparticles after calcination at elevated temperatures (700 °C). X-ray diffraction (XRD) and transmission electron microscopic (TEM) measurements showed that the SnO₂ particles exhibited high crystallinity with a rutile structure, and spherical Au nanoparticles were dispersed on the surface of the SnO₂ support. Based on the TEM images and the width of the Au(2 0 0) XRD diffraction peak, the size of the Au nanoparticles was found to be between 15 and 35 nm in diameter and decrease with increasing loading of the original HAuCl₄ precursor. The electrocatalytic activity of the resulting SnO₂–Au($x$) composite nanoparticles toward oxygen reduction reactions (ORR) was then evaluated by cyclic and rotating disk voltammetric measurements in alkaline solutions. It was found that the incorporation of gold nanoparticles led to apparent improvement of the catalytic activity of SnO₂ nanoparticles. Moreover, the ORR electrocatalytic activity exhibited a strong dependence on the gold loading in the hybrid nanoparticles, and the most active catalyst was found with a gold loading of 1.9 at.%, based on the reduction current density and onset potential of ORR. Furthermore, at this gold loading, oxygen reduction was found to follow the efficient four-electron reaction pathway, whereas at other Au loadings, the number of electron transfer involved in oxygen reduction varied between 1 and 3. Additionally, Tafel analysis suggested that at low overpotentials, the first electron transfer might be the limiting step in oxygen reduction, whereas at high potentials, oxygen adsorption appeared to play the determining role at the SnO₂–Au hybrid electrodes. These results indicate that the SnO₂–Au composite nanoparticles might serve as effective catalysts for oxygen electroreduction in alkaline media.

© 2009 Elsevier B.V. All rights reserved.

## 1. Introduction

Direct liquid fuel cells have been attracting much attention as potentially green, inexpensive, and efficient power sources for a variety of practical applications, such as electrical vehicles, portable as well as stationary electronic devices, etc. [1,2]. A typical fuel cell is composed of two electrodes, anode for the oxidation of fuel molecules (hydrogen, methanol, formic acid, etc.) and cathode where the reduction of oxygen occurs. Yet, despite substantial improvements of fuel cell performance in recent years, the widespread commercialization of fuel cells has been impeded by several challenging obstacles. Of these, one major issue is related to the cathodic reactions which exhibit significant overpotentials because of the sluggish reaction kinetics. At present, among the metal catalysts used, platinum and platinum-based alloys generally show

the highest catalytic activity for both anode and cathode reactions [3–8]. However, platinum is costly and of limited reserve. Therefore, recently extensive research efforts have also been devoted to the development of non-Pt electrocatalysts for fuel cell electrochemistry, including transition metal oxides [9,10], transition metal sulfides [11], transition metal macrocyclic complexes [12,13], and metal-containing porphyrin systems [14].

Of these Pt-free electrocatalysts, transition metal oxides are attracting much attention as a kind of efficient electrode catalysts for oxygen reduction reactions (ORR) because of their long-term chemical stability, high photocatalytic activity, and low-cost synthesis. For instance, titanium dioxides are widely used for ORR in both acidic and alkaline media, with a high overpotential [15–19]. Mentus [10] studied ORR on anodically formed TiO₂ in both alkaline and acidic solutions and found that the reactions followed the direct 4e⁻ reduction pathway in alkaline media, whereas in acidic media, the inefficient 2e⁻ reduction pathway was favored. Similarly, tin oxides have also been evaluated as potential cathode catalysts for fuel cell reactions, although the study is relatively scarce. For instance, Liu et al. recently observed that titanium oxide

and tin oxide films made by sputtering methods displayed rather comparable activity for oxygen reduction [9]. Furthermore, tin oxide supported Au and Pt nanoparticles have also been found to act as effective catalysts for oxygen reduction [20–23].

In the present study, we examine the electrocatalytic activity of a series of SnO$_2$–Au hybrid nanoparticles in the electroreduction of oxygen. The SnO$_2$ nanoparticles were first synthesized in a single step by electrochemical oxidation of a tin metal sheet in a non-aqueous electrolyte. Then a controlled amount of HAuCl$_4$ was loaded onto the SnO$_2$ nanoparticles. Calcination at elevated temperatures led to the formation of Au nanoparticles that were dispersed onto the SnO$_2$ surfaces. The structures of the SnO$_2$–Au hybrid nanoparticles were characterized by X-ray diffraction (XRD) and transmission electron microscopy (TEM) measurements. The electrocatalytic activities of these functional nanocomposites for oxygen reduction were then investigated by cyclic voltammetry and rotating disk voltammetry in alkaline solutions.

## 2. Experimental

### 2.1. Materials

Tin foil (0.25 mm thick, 99.8% purity (metal basis)) and ethylene glycol (99+%) were purchased from Aldrich. Ammonium fluoride (NH$_4$F, 98+%, extra pure), potassium perchlorate (KClO$_4$, 98%), and sodium hydroxide (NaOH, 86%) were purchased from ACROS. Hydrogen tetrachloroauric acid (HAuCl$_4$) was synthesized by dissolving ultra-high purity gold (99.999%, Johnson Matthey) in freshly prepared aqua regia. Water was supplied by a Barnstead Nanopure water system (18.3 MΩ cm). Ultrapure N$_2$ and O$_2$ were used for the deaeration of the electrolyte solutions and oxygen reduction reactions, respectively. All other chemicals were purchased from typical commercial sources and used without further treatment.

### 2.2. Sample preparation

SnO$_2$ nanoparticles were prepared by using a two-electrode cell in which the tin foil was used as the sacrificial anode and a Pt coil as the cathode, along with a non-aqueous electrolyte consisting of NH$_4$F in ethylene glycol [24]. Before the experiments, the tin sheet was decreased by sonication in acetone, ethanol, and Nanopure water successively and then dried in nitrogen. The electrochemical reactions were carried out at room temperature using a DC regulated power supply (B&K Precision Corp., 1623A, output voltage 0–60 V) in the constant voltage mode with the applied voltage at 30 V. After the reactions, the resulting white powders were centrifuged and thoroughly washed with Nanopure water and absolute ethanol for several times and dried at room temperature, affording purified SnO$_2$ nanoparticles.

0.4 mg of the prepared SnO$_2$ nanoparticles was then added into 10 mL of an aqueous solution of HAuCl$_4$ at different concentrations (varying from 0.25, 1, 2, 5, 8, to 10 mM), and the mixture was under vigorous stirring overnight. The Au-loaded tin oxide powders were then centrifuged and thoroughly washed with Nanopure water. The dried powders were finally calcined in air at 700 °C for 6 h with the heating and cooling rates controlled at 5 °C min$^{-1}$. Assuming that all Au was converted into gold nanoparticles and dispersed onto the SnO$_2$ surface, the gold loading (atom ratio, $x$) was evaluated to be 0.095, 0.38, 0.76, 1.9, 3.0, and 3.8 at.%. The resulting hybrid particles were denoted as SnO$_2$–Au($x$).

### 2.3. Electrochemistry

A glassy carbon (GC) disk electrode (Bioanalytical Systems, diameter 3.0 mm) was first polished with alumina slurries (0.05 μm) and then cleaned by sonication in 0.1 M HNO$_3$,

0.1 M H$_2$SO$_4$, and Nanopure water for 10 min successively. The SnO$_2$–Au($x$) hybrid particles prepared above were then deposited onto the cleaned GC electrode surface by adopting a literature procedure [24]. Briefly, 1 mg of the particles was dispersed ultrasonically in a mixture of 700 μL of pure water and 60 μL of 5 wt.% Nafion solution. After the formation of a homogeneous ink, 8 μL of the catalyst ink was dropcast onto the GC electrode surface with a micropipette and then dried in air. The electrodes were denoted as SnO$_2$–Au($x$)/GC.

All electrochemical experiments were performed using a standard three-electrode configuration. A Ag/AgCl (in 3 M NaCl, aq) (Bioanalytical Systems, MF-2052) and a Pt coil were used as the reference and counter electrodes, respectively. All electrode potentials in the present study were referred to this Ag/AgCl reference electrode. Cyclic voltammetry and rotating disk voltammetry were carried out using a computer-controlled Bioanalytical Systems (BAS) Electrochemical Analyzer (Model 100B). Oxygen reduction reactions were examined by first bubbling the electrolyte solution with ultra-high purity oxygen for at least 15 min and then blanketing the solution with an oxygen atmosphere during the entire experimental procedure. All electrochemical experiments were carried out at room temperature.

### 2.4. XRD and TEM characterizations

Powder X-ray diffraction (XRD) measurements were performed with a Rigaku Mini-flex Powder Diffractometer using Cu Kα radiation with a Ni filter ($\lambda = 0.154059$ nm at 30 kV and 15 mA) which features a detection limit of 0.04°. The particle size and morphology of the Au-doped SnO$_2$ particles were examined with a JEOL 1200 EX transmission electron microscope (TEM) at 80 keV. The samples were prepared by casting a drop of the particle solution ($\sim$1 mg mL$^{-1}$) in ethanol onto a 200-mesh carbon-coated copper grid.

## 3. Results and discussion

### 3.1. Structural characterizations

To examine the crystallinity of the SnO$_2$–Au($x$) hybrid particles, powder X-ray diffraction measurements were first carried out. Fig. 1(A) shows the XRD patterns of the SnO$_2$ nanoparticles decorated with varied amounts of Au ($x = 0$, 0.095, 0.38, 0.76, 1.9, 3.0, and 3.8 at.%, corresponding to curves (b)–(h), respectively) after thermal calcination at 700 °C. The JCPDS data of SnO$_2$ (cassiterite, No. 41-1445) are also included in the figure as curve (a). It can be seen that all the samples show clear, sharp, and strong diffraction peaks that are in excellent agreement with the tetragonal structure (rutile type) of SnO$_2$ (curve a), with the lattice constants of $a = 4.738$ Å and $c = 3.187$ Å. The observed XRD patterns strongly indicate that the heat-treated particles exhibit high crystallinity (indeed high-resolution TEM studies show very well-defined crystalline lattices [24]). Additionally, no diffraction peaks from impurities such as unreacted tin and tin oxides of other crystalline phases are observed, suggesting the purity of the rutile SnO$_2$ structures. Furthermore, the average size of the SnO$_2$ particles may be estimated by the Debye–Scherrer equation, $D = K\lambda/\beta \cos\theta$, where $D$ is the diameter of the nanoparticles, $K = 0.9$, $\lambda$(Cu Kα) = 1.54059 Å, and $\beta$ is the full width at half maximum (FWHM) of the diffraction peaks. Based on the SnO$_2$ (1 1 0) and (1 0 1) diffraction peaks, the average size of the SnO$_2$ particles was estimated to be 20 nm.

The diffraction patterns of gold nanoparticles were found at $2\theta$ between 40 and 50° (dashed box in panel A, which is magnified in panel B). It can be seen that with increasing gold loading, the diffraction peaks at ca. 44.5°, which are ascribed to the Au(2 0 0) crystalline
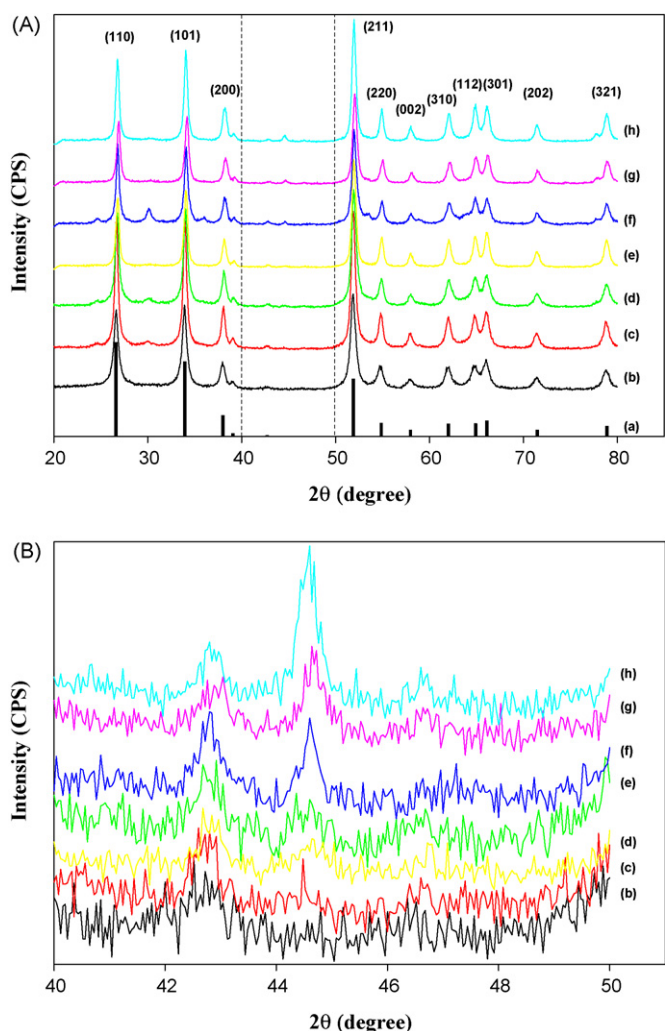
**Fig. 1.** (A) XRD patterns of (a) bulk $SnO_2$ from the Joint Committee Powder Diffraction Standard (JCPDS) No. 41-1445; (b) pure $SnO_2$ nanoparticles and $SnO_2$ particles loaded with different Au contents: (c) 0.095 at.%, (d) 0.38 at.%, (e) 0.76 at.%, (f) 1.9 at.%, (g) 3.0 at.%, and (h) 3.8 at.%. All the $SnO_2$ particles were synthesized at 30 V and calcined in air at 700 °C. The XRD patterns with $2\theta$ in the range of 40–50° (dashed box) were magnified in panel (B) to display the diffraction peak from Au particles (at 44.5°).

are about 34.5 nm in diameter whereas at $x = 3.8$ at.%, the diameter diminishes drastically to 18.0 nm.

The hybrid nanoparticles were further analyzed by TEM measurements. Fig. 2 shows the representative TEM micrographs of $SnO_2$ nanoparticles loaded with different Au contents. It can be seen that after calcination at 700 °C, Au nanoparticles appeared to form large agglomerates on the surface of the $SnO_2$ support. Yet, based on the small number of nanoparticles that were recognizable outside of these aggregates (highlighted by red circles in Fig. 2), one can see that the Au nanoparticles exhibit mostly spherical shape, and the core diameter decreases with increasing Au loading in the nanocomposites, similar to the trend observed in XRD measurements (Table 1). For instance, at $x = 0.095$ at.%, the diameter of the gold particles is about 29.3 nm whereas at $x = 3.8$ at.%, it decreases drastically to 15.2 nm. This may be accounted for by the growth mechanism of gold nanoparticles. At higher Au salt concentrations, more Au nuclei would be formed in a short period of time, leading to the suppression of the growth of Au nanoparticles and hence smaller particles as the final products.

From Table 1, one might note that the particle core sizes obtained from XRD measurements are somewhat larger than those evaluated from TEM measurements. This discrepancy may be, at least partly, ascribed to the relatively weak Au(200) diffraction peaks in XRD patterns, which renders it difficult to have an accurate assessment of the peak width, in particular, at low Au loadings.

### 3.2. Cyclic voltammetry

The electrocatalytic activity of the $SnO_2$–Au($x$)/GC electrodes for oxygen reduction was then evaluated by cyclic voltammetry in alkaline solutions. Fig. 3 shows representative cyclic voltammograms of the $SnO_2$–Au(0.095 at.%)/GC electrode in an aqueous electrolyte of 0.02 M NaOH + 0.2 M $KClO_4$ (pH 12.2) that was saturated either with $N_2$ or $O_2$ within the potential range of +0.6 to −0.7 V. It can be seen that when the electrolyte solution was saturated with $N_2$ the voltammetric response was essentially featureless (dashed curve). In contrast, in the $O_2$-saturated solution, the cathodic current increased significantly (solid curve), with a well-defined peak at ca. −0.45 V, indicative of apparent electrocatalytic activity of the nanocomposite for oxygen reduction. The figure inset shows the cathodic peak current ($I_p$) as a function of the square root of potential sweep rate. The linearity of the plot is consistent with the typical feature of diffusion-controlled oxygen reduction reactions. Similar behaviors were also observed with other $SnO_2$–Au($x$)/GC electrodes.

Fig. 4 shows the voltammograms for oxygen reduction at the $SnO_2$–Au($x$)/GC electrodes with different Au loading ($x$ ranging from 0 to 3.8 at.%). On the basis of cathodic current density and onset potential for oxygen reduction, at least two conclusions can be drawn: (i) the catalytic activity for ORR is improved with the $SnO_2$–Au hybrid nanoparticles in comparison to the

lattice, become increasingly visible. This confirms the presence and crystallinity of the Au nanoparticles in the hybrid nanomaterials. Interestingly, the average diameter of the gold nanoparticles, as estimated by the Debye–Scherrer equation based on the Au(200) diffraction peak, decreases monotonically with increasing Au contents (Table 1). For instance, at $x = 0.095$ at.%, the gold particles

**Table 1**
Average size of Au nanoparticles evaluated from XRD and TEM measurements.

| Au loading ($x$, at%) | 0 | 0.095 | 0.38 | 0.76 | 1.9 | 3.0 | 3.8 |
|---|---|---|---|---|---|---|---|
| Particle size evaluated from XRD (nm)[a] | 20 | 34.5 | 33.0 | 30.4 | 27.2 | 20.4 | 18.0 |
| Particle size evaluated from TEM (nm)[b] | | 29.3 | 27.5 | 27.3 | 25.3 | 17.7 | 15.2 |
| Number of electron transferred ($n$)[c] | 1.0 | 1.3 | 1.8 | 2.6 | 4.1 | 3.2 | 3.0 |
| Onset potential (V)[d] | −0.24 | −0.21 | −0.23 | −0.11 | +0.06 | −0.12 | −0.11 |
| Current density at −0.3 V (mA cm$^{-2}$)[d] | −0.06 | −0.08 | −0.08 | −0.16 | −0.41 | −0.24 | −0.15 |
| Tafel slopes (mV/dec)[e] | −119.5 | −147.4 | −161.4 | −230.2 | −259.6 | −201.2 | −239.4 |
| | −330.6 | −2028.6 | −332.6 | −570.2 | −653.9 | −434.6 | −423.8 |

[a] The average size was evaluated from the Au(200) diffraction peak of the XRD patterns as shown in Fig. 1(B).

[b] The average size was evaluated from the TEM images as shown in Fig. 2.

[c] The numbers of electron transferred for ORR were calculated from Eqs. (1) and (2) by curve fitting of the Koutecky–Levich plots (Fig. 5(B)).

[d] Onset potential and current density at −0.3 V were obtained from the rotating disk voltammograms at the rotation rate of 225 rpm (Fig. 6(A)).

[e] The Tafel slopes at the low and high current density regions were listed at the top and bottom, respectively (Fig. 6(B)).
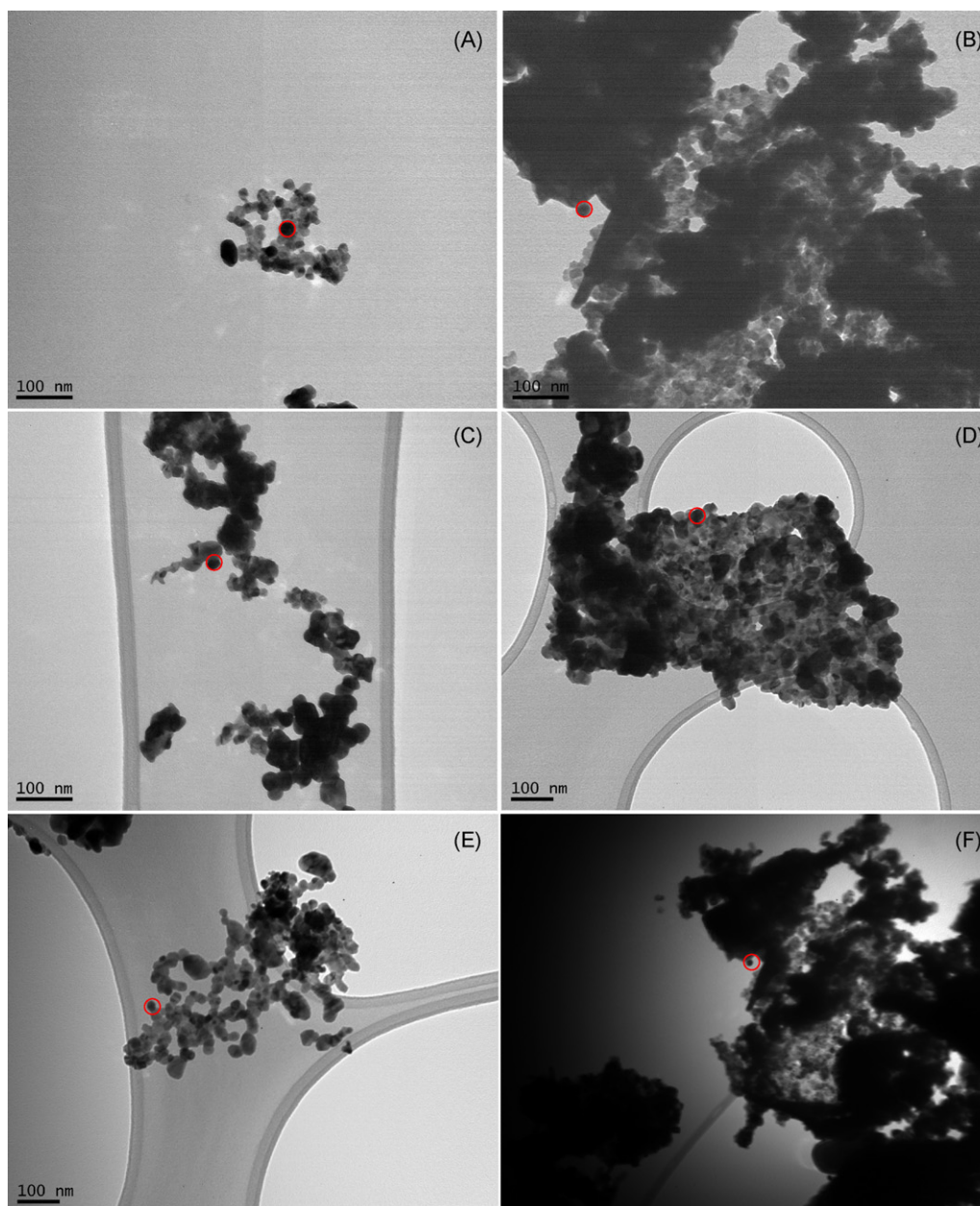
**Fig. 2.** TEM images of SnO$_2$ nanoparticles loaded with different Au content: (A) 0.095 at.%, (B) 0.38 at.%, (C) 0.76 at.%, (D) 1.9 at.%, (E) 3.0 at.%, and (F) 3.8 at.%. The red circle in each image shows the representative Au nanoparticles formed after calcination of the samples at 700 °C. Scale bars are all 100 nm. (For interpretation of the references to color in this figure caption, the reader is referred to the web version of the article.)

SnO$_2$ nanoparticles alone (i.e., $x = 0$) and (ii) the SnO$_2$–Au(1.9 at.%) sample appears to exhibit the best catalytic performance within the series. For instance, the cathodic peak current density at the SnO$_2$/GC electrode is $-0.57$ mA cm$^{-2}$, whereas it increases rather markedly to $-2.19$ mA cm$^{-2}$ at the SnO$_2$–Au(1.9 at.%)/GC electrode. Additionally, the onset potential for oxygen reduction at the SnO$_2$–Au(1.9 at.%)/GC electrode (+0.06 V) is substantially more positive than that at the SnO$_2$/GC electrode ($-0.24$ V). Such enhancement of the electrocatalytic activity has also been observed with other metal oxide materials loaded with precious or non-precious metal nanoparticles [20,23,25,26].

Bulk gold is usually considered to be a poor electrocatalyst for oxygen reduction (for instance, as manifested by the dashed curve in Fig. 4), because of the low affinity to oxygen adsorption and the difficulty of donating electrons to O$_2$ to form O$_2^-$. However, at the SnO$_2$–Au hybrid nanoparticles, according to the bifunctional mech-anism proposed by Baker et al. [21], chemisorption of O$_2$ onto the SnO$_2$ surface as O$_2^-$ may be facilitated by Sn$^{2+}$ ions produced by cathode polarization. Further reduction of O$_2^-$ to H$_2$O may then be catalyzed by Au nanoparticles.

### 3.3. Rotating disk voltammetry

The dynamics of oxygen reduction by the SnO$_2$–Au hybrid nanocatalysts were then examined as a function of the cata-lyst composition by rotating disk voltammetry. Fig. 5 shows a series of rotating disk voltammograms of oxygen reduction at two SnO$_2$–Au/GC electrodes, $x = 0.095$ at.% (A) and 1.9 at.% (B), at differ-ent rotation rates in an aqueous solution of 0.02 M NaOH + 0.2 M KClO$_4$ (pH 12.2) saturated with O$_2$. Note that the background current acquired with a nitrogen-saturated solution has been sub-tracted from the voltammetric currents at the respective electrode.
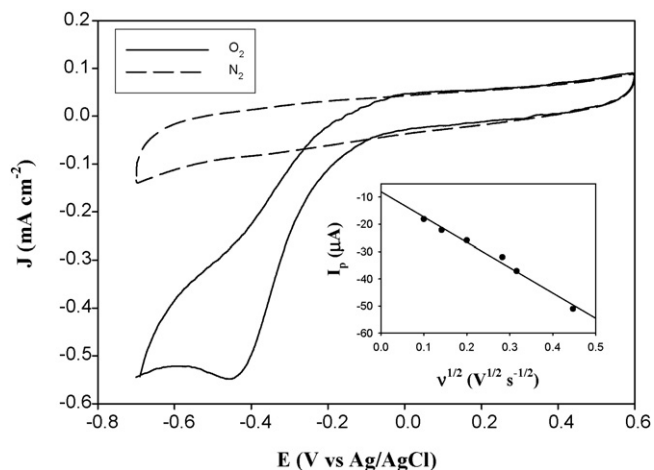
**Fig. 3.** Cyclic voltammograms of the $SnO_2$–Au (0.095 at.%)/GC electrode in an aqueous solution of 0.02 M NaOH + 0.2 M $KClO_4$ (pH 12.2) that was saturated either with $N_2$ (dashed curve) or with $O_2$ (solid curve). Potential sweep rate 100 mV s$^{-1}$. Inset depicts the variation of the cathodic peak current ($I_p$) of oxygen reduction with the square root of potential sweep rate. Symbols are experimental data and line is liner regression.

It can be seen that the limiting current density increases with increasing rotation rate. Again, similar voltammetric features were also observed with other $SnO_2$–Au($x$)/GC electrodes, suggesting the apparent activity of the hybrid nanoparticles towards oxygen reduction.

For oxygen reduction on a rotating disk electrode (RDE), the current density can be described by the Koutecky–Levich equation:

$$\frac{1}{J} = \frac{1}{J_K} + \frac{1}{J_L} = \frac{1}{J_K} + \frac{1}{B\omega^{1/2}} \quad (1)$$

$$B = 0.62nFC_O D_O^{2/3} \nu^{-1/6} \quad (2)$$

$$J_K = nFkC_O \quad (3)$$

where $J$ is the measured current density, $J_K$ and $J_L$ are the kinetic and diffusion limiting current density, respectively, $\omega$ is the electrode rotation rate, $n$ is the overall number of electron transfer, $F$ is the Faraday constant, $C_O$ is the bulk concentration of $O_2$ dissolved in the electrolyte, $D_O$ is the $O_2$ diffusion coefficient, and $\nu$ is the kinematic viscosity of the electrolyte. Therefore, based on
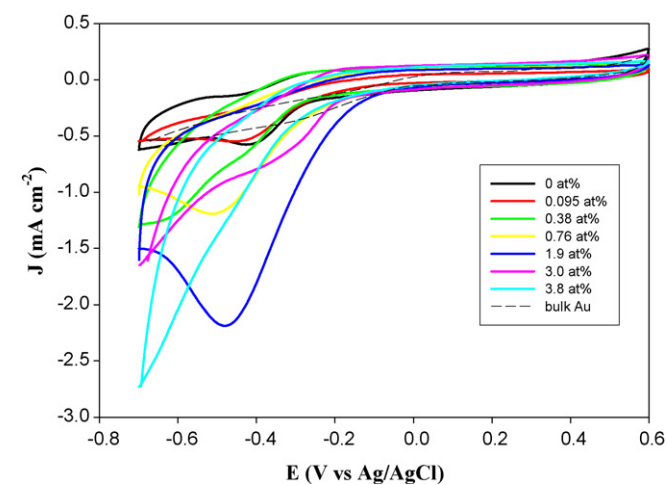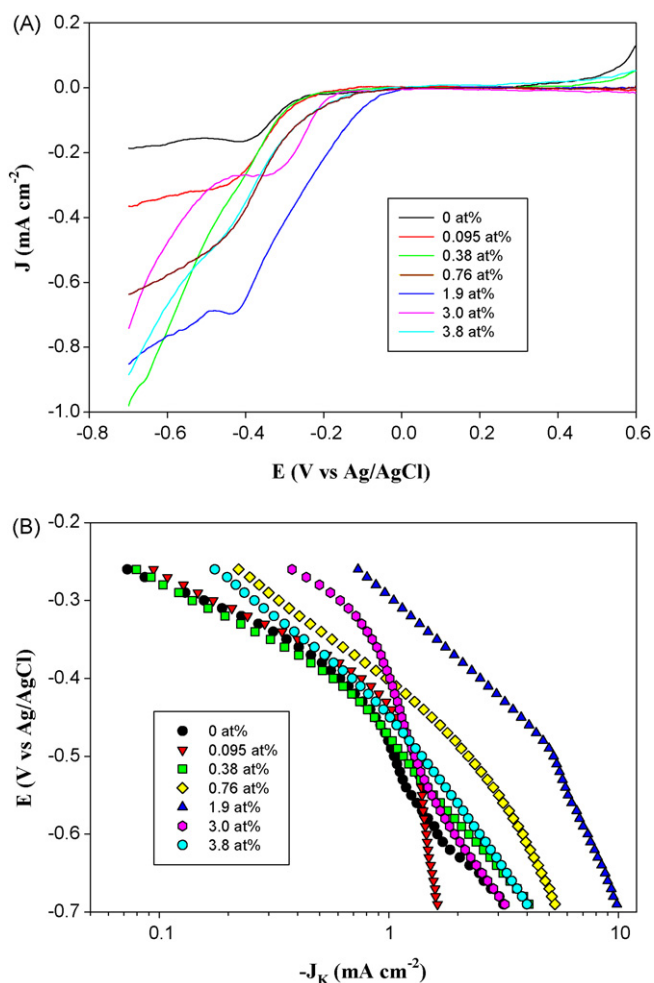


**Fig. 4.** Cyclic voltammograms of the $SnO_2$–Au($x$)/GC electrodes with different Au loadings (shown as figure legends) in an aqueous solution of 0.02 M NaOH + 0.2 M $KClO_4$ (pH 12.2) that was saturated with oxygen. The voltammogram at a bulk Au electrode was also included in the figure (dashed curve). Potential sweep rate 100 mV s$^{-1}$.
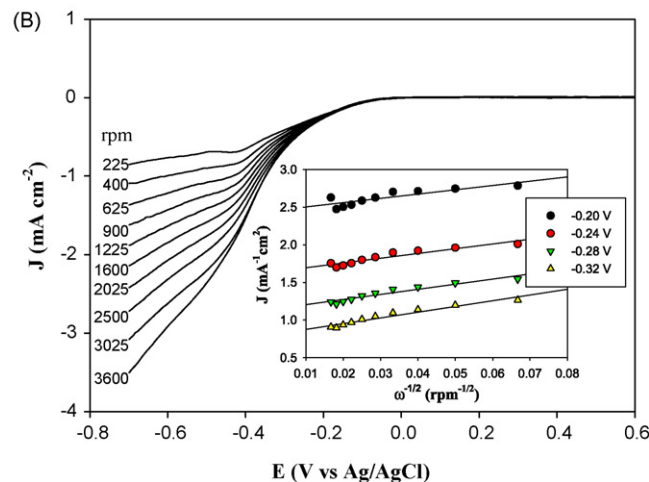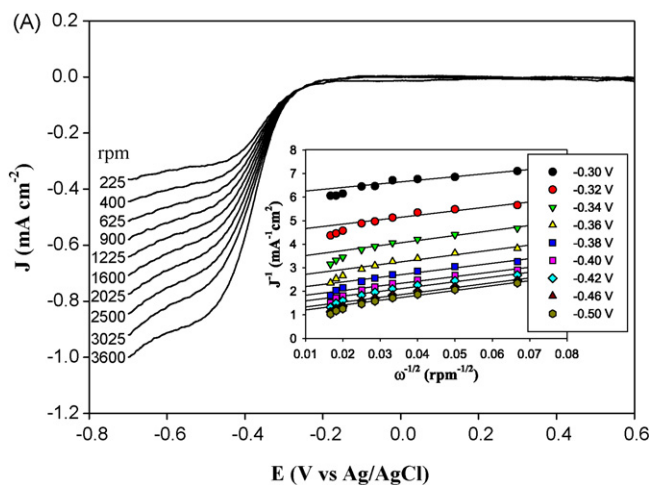




**Fig. 5.** Rotating disk voltammograms for (A) $SnO_2$–Au(0.095 at.%)/GC and (B) $SnO_2$–Au(1.9 at.%)/GC electrode in an oxygen-saturated aqueous solution of 0.02 M NaOH + 0.2 M $KClO_4$ (pH 12.2) at different rotation rates (shown as figure legends). Note that the voltammetric currents acquired in a nitrogen-saturated solution using the same electrodes have been subtracted from the respective voltammograms. DC ramp 20 mV s$^{-1}$. Insets show the corresponding Koutecky–Levich plots ($J^{-1}$ vs. $\omega^{-0.5}$) at different electrode potentials (shown as figure legends). Symbols are experimental data obtained from the voltammograms and lines are the linear regressions.

the Koutecky–Levich equation, a plot of the inverse of the current density ($J^{-1}$) versus $\omega^{-1/2}$ should yield a straight line with the intercept corresponding to $J_K$ and the slopes reflecting the so-called $B$ factor (Eq. (2)). The number of electron transfer in the $O_2$ reduction process can then be calculated from the $B$ factor by using the literature data [27,28] of $C_O = 2.5 \times 10^{-6}$ M, $D_O = 1.9 \times 10^{-5}$ cm$^2$ s$^{-1}$ and $\nu = 9.97 \times 10^{-5}$ cm$^2$ s$^{-1}$. The figure insets depict the corresponding Koutecky–Levich plots for these two $SnO_2$–Au/GC electrodes. It can be seen that at both electrodes the slopes remain approximately constant over the potential range under study (−0.30 V to −0.50 V), indicating a consistent number of electron transfer for ORR at different electrode potentials. Specifically, based on Eqs. (1) and (2), the number of electron transfer in oxygen reduction ($n$) was estimated to be 1.3 for $x = 0.095$ at.%, suggesting incomplete reduction of oxygen at this electrode, whereas at $x = 1.9$ at.%, $n = 4.1$, indicative of efficient reduction of oxygen into water. The estimation of $n$ for other electrodes was also carried out in a similar manner and the results are summarized in Table 1. It can be seen that for pure $SnO_2$, $n = 1.0$, indicative of poor electrocatalytic activity of $SnO_2$ alone for oxygen reduction. However, upon the loading of Au nanoparticles onto the oxide support, the value of $n$ increases: 1.3 ($x = 0.095$ at.%), 1.8 (0.38 at.%), 2.6 (0.76 at.%), 4.1 (1.9 at.%), 3.2 (3.0 at.%), and 3.0

**Fig. 6.** (A) Representative rotating disk voltammograms and (B) the corresponding Tafel plots of the seven $SnO_2$–Au(x)/GC electrodes (x = 0, 0.095, 0.38, 0.76, 1.9, 3.0, and 3.8 at.%) in an oxygen-saturated aqueous solution of 0.02 M NaOH + 0.2 M KClO$_4$ (pH 12.2). Note that the voltammetric currents acquired in a nitrogen-saturated solution using the same electrodes have been subtracted from the respective voltammograms. Rotation rate 225 rpm, and DC ramp 20 mV s$^{-1}$.

(3.8 at.%). Notably, of these, the $SnO_2$–Au (1.9 at.%)/GC electrode behaves as the optimal catalyst for oxygen reduction which follows a four-electron reaction pathway.

Similar behaviors were observed by comparing the RDE voltammetric features of these different electrodes. Fig. 6(A) depicts the rotating disk voltammograms for ORR at the $SnO_2$–Au(x) electrodes at the rotation rate of 225 rpm. Again, the cathodic current density as well as the onset potential (Table 1) display a variation trend with the loading of gold nanoparticles that is similar to that observed in voltammetric measurements (Fig. 4). For instance, at the $SnO_2$–Au(1.9 at.%)/GC electrode, the current density of ORR at −0.3 V is the highest among the series at −0.41 mA cm$^{-2}$, whereas it decreases to −0.08 mA cm$^{-2}$ (x = 0.095 at.%) and −0.15 mA cm$^{-2}$ (x = 3.8 at.%). With respect to the onset potential of ORR, the $SnO_2$–Au(1.9 at.%) sample also exhibits the best performance at +0.06 V, whereas at other gold loadings a more negative onset potential is observed, for instance, −0.21 V (x = 0.095 at.%) and −0.11 V (x = 3.8 at.%).

Further analysis was carried out with Tafel plots, as shown in Fig. 6(B), where the kinetic current density was estimated from the Koutecky–Levich plots of the respective electrode. First, it can be seen that the $SnO_2$–Au/GC electrode at x = 1.9 at.% clearly stands out among the series of samples, exhibiting the highest kinetic

current density at the same electrode potentials. Second, all electrodes showed two linear regions with distinctly different slopes depending on the kinetic current density. The data are summarized in Table 1, where it can be seen that the Tafel slopes increases with increasing current density at all the seven electrodes with different gold loading. Specifically, in the low current density region, the slopes are within the range of −120 to −260 mV dec$^{-1}$, which is somewhat larger than that observed in a previous study of oxygen reduction at nanostructured gold thin film electrodes supported on glassy carbon (−120 mV dec$^{-1}$) [27], suggesting that in this potential region the first electron transfer to oxygen was the rate-determining step. In contrast, in the high current density region, the slopes increased drastically to the range of −200 to −650 mV dec$^{-1}$ (note that the 0.095 at.% sample exhibited an exceedingly high slope, the origin of which is not clear at this point). The apparent deviation from −120 mV dec$^{-1}$ suggests that at high overpotentials oxygen reduction at the $SnO_2$–Au hybrid electrode might be primarily limited by oxygen adsorption. Similar behaviors were observed in oxygen reduction at Pt and Pt–TiO$_2$ thin film electrodes [29,30]. Furthermore, it can be seen from Table 1 that among the series, the electrode at x = 1.9 at.% exhibited the largest slopes in each current density region, implying that oxygen adsorption might play a significant role in the electroreduction process at this electrode.

It should be noted that in general the electrocatalytic activity of large gold nanoparticles (and bulk gold) for oxygen reduction is very weak. For instance, in a recent study [31], incomplete reduction of oxygen (n ≈ 2) was observed with Au nanoparticles larger than 2 nm in diameter. Yet, in the present study, despite the very large gold particle size (15–35 nm), the $SnO_2$–Au hybrid nanoparticles appeared to be fairly efficient in the electrocatalytic reduction of oxygen (n = 3 to 4) at x ≥ 1.9 at.%. This suggests that the hybridization of Au nanoparticles with $SnO_2$ nanomaterials may be an effective route to the enhancement of the electrocatalytic activity as compared to Au or $SnO_2$ alone, as a consequence of the metal–support interactions [21,32,33].

Comparison with other metal nanoparticle–metal oxide nanocomposite electrocatalysts also shows that the $SnO_2$–Au(x) hybrid nanoparticles exhibit promising catalytic activity. For example, on titanium oxide electrodes [10,16], the onset potential of ORR was found to be around −1.0 V, which is far more negative than those observed with the $SnO_2$–Au(x) catalysts (−0.24 V to +0.06 V for x = 0 to 3.8 at.%, Table 1). Importantly, the onset potential of the $SnO_2$–Au(1.9 at.%) sample (+0.06 V) is comparable to that of TiO$_2$–Pt hybrid catalysts [29,30] which is found around 0.0 V. Onset potential at ca. 0 V was also observed with nanostructured gold thin film electrodes [27]. These results suggest that $SnO_2$–Au hybrid nanoparticles are promising cathode electrocatalysts in alkaline media. Certainly, the performance may be further optimized by the composition and surface engineering of the nanocomposite catalysts, which will be pursued in future work.

## 4. Conclusions

In this study, $SnO_2$–Au hybrid nanoparticles were synthesized and examined as novel electrocatalysts toward oxygen reduction reactions. XRD measurement showed that after calcination at 700 °C the $SnO_2$ particles exhibited a tetragonal rutile structure with an average size of about 20 nm. TEM images revealed that the $SnO_2$ nanoparticles were highly crystalline and the Au nanoparticles were dispersed on the $SnO_2$ surface with the average core diameter varied from 15 to 35 nm. The catalytic activity of the $SnO_2$–Au hybrid nanoparticles for ORR was then studied and compared by cyclic voltammetry and rotating disk voltammetry. The results showed that the electrocatalytic activity of the $SnO_2$–Au

nanocomposites was markedly enhanced as compared to that of the $SnO_2$ nanoparticles alone, and the activity varied sensitively with the loading of the Au content. Importantly, within the present experimental context, the $SnO_2$–Au(1.9 at.%) sample exhibited the best electrocatalytic activity with the highest reduction density and the most positive onset potential, where oxygen reduction followed an efficient four-electron reaction pathway. Additionally, Tafel analysis showed that at low overpotentials, the first electron transfer might be the limiting step in oxygen reduction, whereas at high potentials, oxygen adsorption appeared to play the determining role at the $SnO_2$–Au hybrid electrodes. The present study suggests that $SnO_2$–Au nanocomposite particles may serve as effective non-platinum electrocatalysts in fuel cell reactions in alkaline media.

## Acknowledgments

## References

[1] B.C.H. Steele, A. Heinzel, Nature 414 (2001) 345–352.
[2] R.A. Lemons, Journal of Power Sources 29 (1990) 251–264.
[3] J. Zhang, F.H.B. Lima, M.H. Shao, K. Sasaki, J.X. Wang, J. Hanson, R.R. Adzic, Journal of Physical Chemistry B 109 (2005) 22701–22704.
[4] J. Zhang, K. Sasaki, E. Sutter, R.R. Adzic, Science 315 (2007) 220–222.
[5] U.A. Paulus, A. Wokaun, G.G. Scherer, T.J. Schmidt, V. Stamenkovic, V. Radmilovic, N.M. Markovic, P.N. Ross, Journal of Physical Chemistry B 106 (2002) 4181–4191.
[6] W. Chen, J.M. Kim, S.H. Sun, S.W. Chen, Journal of Physical Chemistry C 112 (2008) 3891–3898.
[7] M.K. Min, J.H. Cho, K.W. Cho, H. Kim, Electrochimica Acta 45 (2000) 4211–4217.
[8] H. Yang, W. Vogel, C. Lamy, N. Alonso-Vante, Journal of Physical Chemistry B 108 (2004) 11024–11034.
[9] Y. Liu, A. Ishihara, S. Mitsushima, N. Kamiya, K. Ota, Journal of the Electrochemical Society 154 (2007) B664–B669.
[10] S.V. Mentus, Electrochimica Acta 50 (2004) 27–32.
[11] J.J. Diao, F.S. Qiu, G.D. Chen, M.E. Reeves, Journal of Physics D: Applied Physics 36 (2003) L25–L27.
[12] H.S. Liu, C.J. Song, Y.H. Tang, J.L. Zhang, H.J. Zhang, Electrochimica Acta 52 (2007) 4532–4538.
[13] L. Zhang, J.J. Zhang, D.P. Wilkinson, H.J. Wang, Journal of Power Sources 156 (2006) 171–182.
[14] A. Scholze, A. Schenk, W. Fichtner, IEEE Transactions on Electron Devices 47 (2000) 1811–1818.
[15] S.K. Poznyak, A.I. Kokorin, A.I. Kulak, Journal of Electroanalytical Chemistry 442 (1998) 99–105.
[16] V.B. Baez, J.E. Graves, D. Pletcher, Journal of Electroanalytical Chemistry 340 (1992) 273–286.
[17] A. Tsujiko, H. Itoh, T. Kisumi, A. Shiga, K. Murakoshi, Y. Nakato, Journal of Physical Chemistry B 106 (2002) 5878–5885.
[18] Y.K. Choi, S.S. Seo, K.H. Chjo, Q.W. Choi, S.M. Park, Journal of the Electrochemical Society 139 (1992) 1803–1807.
[19] B. Parkinson, F. Decker, J.F. Juliao, M. Abramovich, H.C. Chagas, Electrochimica Acta 25 (1980) 521–525.
[20] M. Watanabe, S. Venkatesan, H.A. Laitinen, Journal of the Electrochemical Society 130 (1983) 59–64.
[21] W.S. Baker, J.J. Pietron, M.E. Teliska, P.J. Bouwman, D.E. Ramaker, K.E. Swider-Lyons, Journal of the Electrochemical Society 153 (2006) A1702–A1707.
[22] T. El Moustafid, H. Cachet, B. Tribollet, D. Festy, Electrochimica Acta 47 (2002) 1209–1215.
[23] M.S. Saha, R.Y. Li, M. Cai, X.L. Sun, Electrochemical and Solid State Letters 10 (2007) B130–B133.
[24] W. Chen, D. Ghosh, S.W. Chen, Journal of Materials Science 43 (2008) 5291–5299.
[25] K. Tammeveski, T. Tenno, A. Rosental, P. Talonen, L.S. Johansson, L. Niinisto, Journal of the Electrochemical Society 146 (1999) 669–676.
[26] J.M. Macak, F. Schmidt-Stein, P. Schmuki, Electrochemistry Communications 9 (2007) 1783–1787.
[27] A. Sarapuu, M. Nurmik, H. Mandar, A. Rosental, T. Laaksonen, K. Kontturi, D.J. Schiffrin, K. Tammeveski, Journal of Electroanalytical Chemistry 612 (2008) 78–86.
[28] R.E. Davis, G.L. Horvath, C.W. Tobias, Electrochimica Acta 12 (1967), 287–&.
[29] K. Tammeveski, T. Tenno, J. Claret, C. Ferrater, Electrochimica Acta 42 (1997) 893–897.
[30] K. Tammeveski, M. Arulepp, T. Tenno, C. Ferrater, J. Claret, Electrochimica Acta 42 (1997) 2961–2967.
[31] W. Chen, S.W. Chen, Angewandte Chemie: International Edition 48 (2009) 4386–4389.
[32] M. Gustavsson, H. Ekstrom, R. Hanarp, L. Eurenius, G. Lindbergh, E. Olsson, B. Kasemo, Journal of Power Sources 163 (2007) 671–678.
[33] J. Shim, C.R. Lee, H.K. Lee, J.S. Lee, E.J. Cairns, Journal of Power Sources 102 (2001) 172–177.